ACS APPLIED MATERIALS & INTERFACES

Research Article

Cite This: ACS Appl. Mater. Interfaces 2018, 10, 38326−38333

www.acsami.org

Sensitive and Robust Ultraviolet Photodetector Array Based on Self-Assembled Graphene/C_{60} Hybrid Films

Shuchao Qin,[†] Xiaoqing Chen,[†] Qianqian Du,[†] Zhonghui Nie,[†] Xinran Wang,[†] Hai Lu,[†] Xizhang Wang,[‡] Kaihui Liu,[§] Yongbing Xu,[†] Yi Shi,[†] Rong Zhang,*[,†] and Fengqiu Wang*[,†]

[†]School of Electronic Science and Engineering, Collaborative Innovation Center of Advanced Microstructures and [‡]School of Chemistry and Chemical Engineering, Nanjing University, 163 Xianlin Avenue, Nanjing 210093, China

[§]State Key Laboratory for Mesoscopic Physics, Collaborative Innovation Center of Quantum Matter, and School of Physics, Peking University, Beijing 100871, China

Supporting Information

ABSTRACT: Graphene has been widely investigated for use in high-performance photodetectors due to its broad absorption band and high carrier mobility. While exhibiting remarkably strong absorption in the ultraviolet range, the fabrication of a large-scale integrable, graphene-based ultraviolet photodetector with long-term stability has proven to be a challenge. Here, using graphene as a template for C_{60} assembly, we synthesized a large-scale all-carbon hybrid film with inherently strong and tunable UV aborption. Efficient exciton dissociation at the heterointerface and enhanced optical absorption enables extremely high photoconductive gain, resulting in UV photoresponsivity of ~10^7 A/W. Interestingly, due to the electron−hole recombination process at the heterointerface, the response time can be modulated by the gate voltage. More importantly, the use of all-carbon hybrid materials ensures robust operation and further allows the demonstration of an exemplary 5 × 5 (2-dimensional) photodetector array. The devices exhibit negligible degradation in figures of merit even after 2 month of operation, indicating excellent environmental robustness. The combination of high responsivity, reliability, and scalable processability makes this new all-carbon film a promising candidate for future integrable optoelectronics.

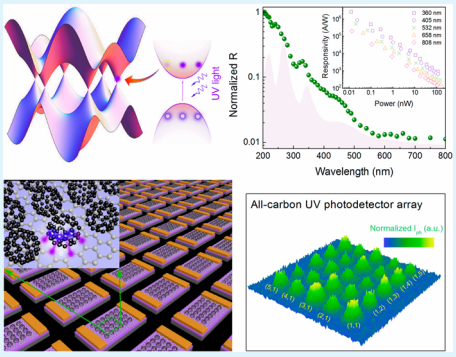

KEYWORDS: *graphene, C_{60}, self-assembled, charge transfer, ultraviolet photodetector*

INTRODUCTION

Atomically thin graphene has attracted intense attention as a promising candidate for electronics and optoelectronics due to its exceptional transport and optical properties.[1,2] The absorption spectrum of graphene, extending from ultraviolet to the far-infrared range, allows the fabrication of ultra-broadband photodetectors. In particular, the pronounced photon absorption near the saddle-point singularity makes graphene well suited for ultraviolet (UV) detector.[3] However, for graphene photodetectors without a gain mechanism, external quantum efficiency (EQE) and responsivity that are too small hamper its practical exploitation.[4,5] In the past few years, highly responsive graphene photodetectors have been demonstrated primarily by employing hybrid systems or interfacial engineering.[6−9] However, nearly all efforts focus on the visible and infrared range, leaving the potential of graphene in the UV band unexplored. On the one hand, this is due to the modest bandgap of most light harvesters, such as transition-metal dichalcogenides (TMDs),[10,11] organic molecules,[6] and quantum-dots (QDs).[7] On the other hand, the high photon energy of UV irradiation can induce damage for a range of functional materials that in turn leads to drastically compromised operation lifetime or durability.[12] As a result, current UV photodetectors are mostly made from inorganic semiconductors such as GaN, ZnO, β-Ga_2O_3, and $NiPS_3$, but these sensing schemes suffer from either low responsivity or high costs.[13−17] A sensitive, robust, and cost-effective alternative with the potential of wafer-scale processing is highly desirable.

Integrating graphene with semiconducting light harvesters proves a capable method for responsivity enhancement using the photogating effect. All-carbon hybrid films have recently shown excellent reliability and superior optoelectronic properties in harvesting excitons.[18−20] Fullerene (C_{60}), a zero-dimensional (0D) carbon allotrope, presents numerous exciting chemical and physical properties and has been widely employed as an efficient trapping material in various optoelectronic applications.[21−24] The strong and tunable absorption of UV light by C_{60} molecules opens up the potential for forming UV functional composite with graphene in a synergetic way. In addition, both theoretical and experimental evidence support the presence of highly efficient

Received: July 11, 2018
Accepted: September 12, 2018
Published: September 12, 2018

DOI: 10.1021/acsami.8b11596
ACS Appl. Mater. Interfaces 2018, 10, 38326−38333

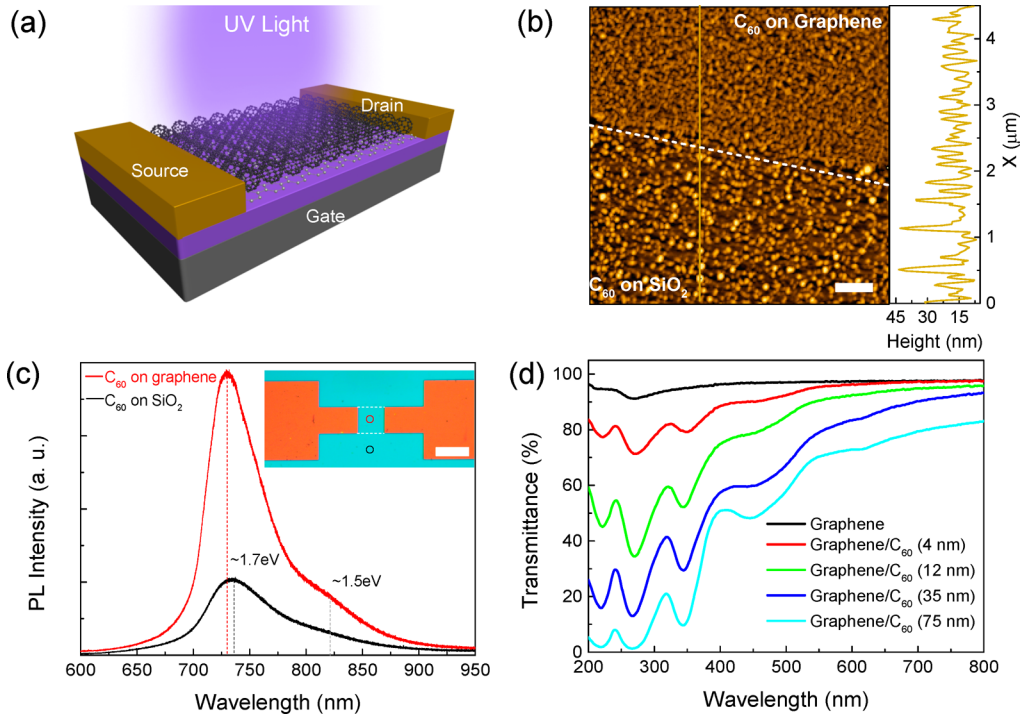

Figure 1. Self-assembled graphene/C_{60} hybrid film. (a) Schematic of the graphene/C_{60} phototransistor on SiO_2/Si. (b) AFM image of a graphene/C_{60} hybrid film on SiO_2/Si substrate. Scale bar: 500 nm. The white dot line marks the boundary of areas with and without graphene. The right panel shows the height profile along the brown solid line. (c) Photoluminescence spectra of C_{60} film (~75 nm) measured at two locations on graphene (red circle, optical microscopy image in inset) and on SiO_2 (black circle). Scale bar: 20 μm. The PL from C_{60} film on graphene is much stronger with a slight blue-shifted peak, indicating better crystalline structure. (d) The absorbance curves of graphene and different graphene/C_{60} hybrid films on quartz, showing tunable UV absorption.

charge transfer at the graphene−C_{60} interface,[25,26] which is important for fabricating high-performance photodetectors.

Here, we demonstrate a highly sensitive and robust UV photodetector (covering 200−400 nm) based on the graphene−C_{60} heterointerface. Utilizing the template effect of graphene, well-organized assembly of C_{60} molecules facilitates exciton dissociation at the graphene−C_{60} interface, leading to a high photoconductive gain, high EQE, and a UV photosensitivity of $>10^7$ A/W (at a wavelength of 200 nm). Interestingly, the decay time can be modulated by the back-gate voltage V_G, showing an asymmetric dependence on the V_G, which results from the recombination process that is limited by the carrier density in graphene and the interfacial potential barrier height. More importantly, the prominent reliability and compatibility with scalable processing allow the demonstration of an exemplary photodetector array, making such all-carbon system an ideal candidate for future integrable optoelectronic applications.

EXPERIMENTAL SECTION

Fabrication and Characterization of Graphene/C_{60} Hybrid Phototransistor. The graphene samples were grown on copper foil by the chemical vapor deposition (CVD) method, and Raman spectroscopy combined with optical microscope characterizations point to a defect-free single-layer sample. The C_{60} solid (purity of 97% without further purification) was purchased from a commercial supplier. The graphene/C_{60} hybrid phototransistors are fabricated as follows: CVD graphene is transferred onto a Si/SiO_2 (285 nm) wafer using the poly(methyl methacrylate) supported procedures. Subsequently, metal composition (Ti/Pd/Au) as the source and drain electrodes are patterned by standard electron-beam lithography (EBL) techniques using PMMA as a resist and then evaporated by electron beam evaporation. Graphene channel fabrication is patterned by another EBL and oxygen plasma etching. The area of the channel is about 20 μm × 20 μm. The electrical performance of graphene transistors was first assessed before C_{60} fabrication. Finally, C_{60} film was grown onto graphene transistor by a thermal evaporation process. The growth temperature was 450 °C under a 1×10^{-6} Torr vacuum. For clean graphene−C_{60} interfaces, two Au patches were mechanically transferred onto an exfoliated graphene sheet sequentially as source/drain contact electrodes. Photoluminescence mapping was performed with 450 nm LED illumination, and the photoluminescence (PL) signal is collected by a charge-coupled device (CCD) equipped with a 500 nm high-pass filter. Raman and PL measurements were performed in a Horiba Jobin Yvon LabRAM HR 800 system using a 514 nm excitation laser operating at 1 mW, a ×100 objective lens with about 1 μm diameter spot size, and grating of 1800 lines per millimeter with a spectral resolution of about 0.45 cm^{-1}. Atomic force microscopy (AFM) measurements were performed using a NT-MDT Spectrum Instruments AFM operating at room temperature and ambient conditions. Optical absorption spectrum was measured using a Hitachi UV−vis-3310 spectrophotometer.

Electrical and Photoresponse Measurements. Electrical characterizations of the transistors were carried out by the Keithley 2614B in a closed probe station under vacuum (10^{-6} Torr) at room temperature. For photoresponse characterization, we used 360, 405, 532, 658, and 808 nm laser diodes, respectively. The beam is guided through an optical fiber with a FC/PC ferrule and is subsequently incident onto the channel of the devices without focusing. The beam at the device was measured to be Gaussian-shaped with a diameter of about 300 μm. The photocurrent mapping was obtained in air, by scanning over the device using Thorlabs GVS212, and modulated photocurrent signals were amplified and detected using the lock-in (Stanford SR830) technique. Photocurrent mapping was performed under 532 nm laser illumination, which was modulated by a square-wave signal generator source. The ultrafast pump−probe spectroscopy is carried out by a pump−probe setup (see details in section S13 of the Supporting Information). Spectral responsivity was performed

DOI: 10.1021/acsami.8b11596
ACS Appl. Mater. Interfaces 2018, 10, 38326−38333

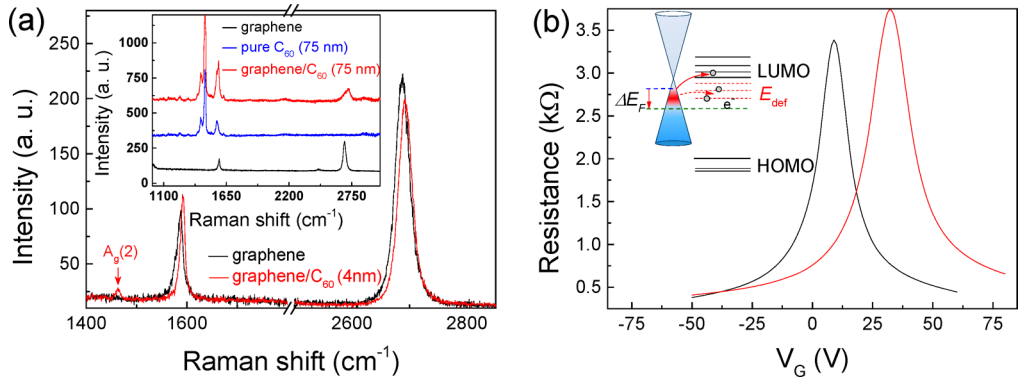

Figure 2. (a) Raman spectra recorded for pristine graphene (black line) and hybrid film after deposition of C_{60} film (~4 nm, red line). The first-order G and second-order 2D Raman features of graphene are identified. The inset shows the Raman spectrum of pristine graphene, pure C_{60} film and graphene/C_{60} hybrid film with a thick C_{60} film (~75 nm). (b) Transfer characteristics of the pristine graphene and graphene/C_{60} transistors. Compared with pristine graphene transistors, the Dirac point of graphene/C_{60} hybrid transistor showed an upshift, indicating p-doping in the graphene sheet induced by C_{60}. The hole (electron) mobility of graphene decreases from 4460 (4720) to 3490 (3100) $cm^2\ V^{-1}\ s^{-1}$ after deposition of C_{60} film due to the scattering induced by C_{60}.

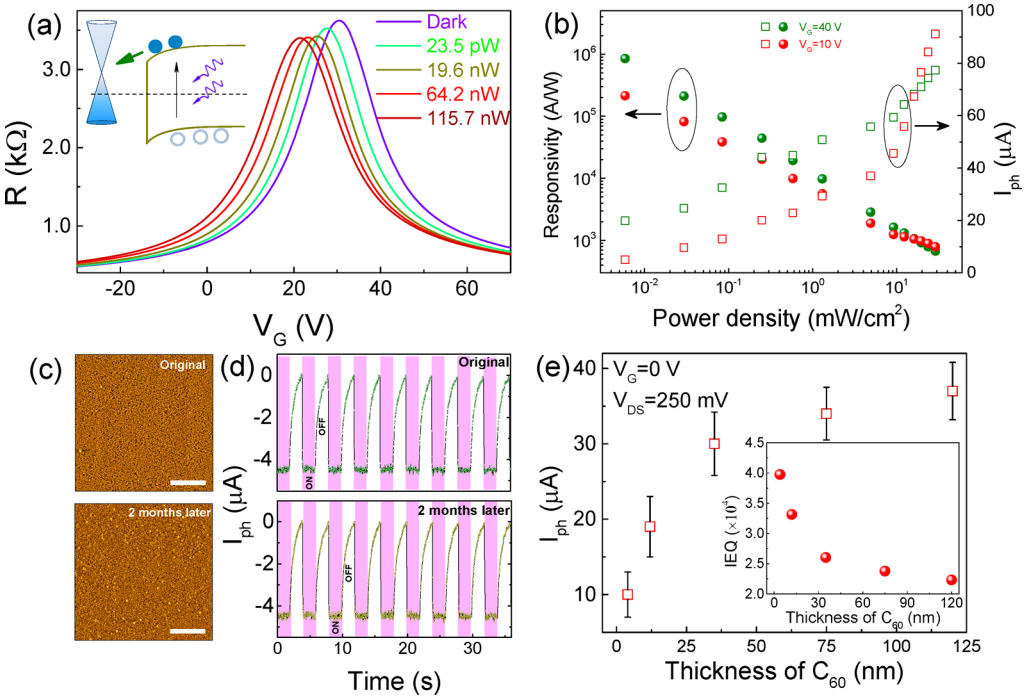

Figure 3. (a) Resistance as a function of gate voltage for the graphene/C_{60} phototransistor under various optical power densities (405 nm laser). Increasing the illumination leads to a photogating effect that shifts the Dirac point to smaller gate voltages. Inset: simplified schematic of charge transfer at the graphene−C_{60} interface. (b) Responsivity (left axis) and photocurrent (right axis) of the hybrid graphene/C_{60} device vs optical illumination power density at different gate biases. (c) AFM images showing the hybrid channel as-made (top panel) and after 2 months in ambient conditions (bottom panel) for the same graphene/C_{60} device. Scale bar: 2 μm. (d) The photocurrent response of the device at V_G = 0 V (hole-dominant regime) as fabricated and after 2 months. Pale light stripes represent the illumination (405 nm). (e) Photocurrents measured with V_G = 0 V and V_{DS} = 250 mV in graphene/C_{60} phototransistors with different C_{60} thicknesses; the illumination power is ~5 mW/cm^2. The inset is the IQE of different graphene/C_{60} hybrid devices.

using a Newport xenon lamp source and spectrophotometer. The incident light intensity was recorded by a power meter (Thorlabs PM100D).

RESULTS AND DISCUSSION

Figure 1a shows the schematic of the CVD graphene/C_{60} phototransistor, which consists of a graphene/C_{60} hybrid channel where the ultrathin fullerene film is deposited onto the CVD-grown graphene via a thermal evaporation process (see the Experimental section for fabrication details). It is worth noting that a higher level of uniformity is achieved on graphene sheet as compared to SiO_2/Si substrate, as revealed by the AFM image (Figure 1b). On the SiO_2/Si substrate, C_{60} molecules underwent island growth mode due to stronger molecules interaction. A more-detailed analysis of the morphologies of C_{60} grown on different substrates confirms that graphene acts an excellent template for depositing well-ordered C_{60} structures (see Figure S1). The PL spectra and PL microscopy of C_{60} film (~75 nm) deposited onto and outside of the graphene substrate verified the well-organized ordered

DOI: 10.1021/acsami.8b11596
ACS Appl. Mater. Interfaces 2018, 10, 38326−38333

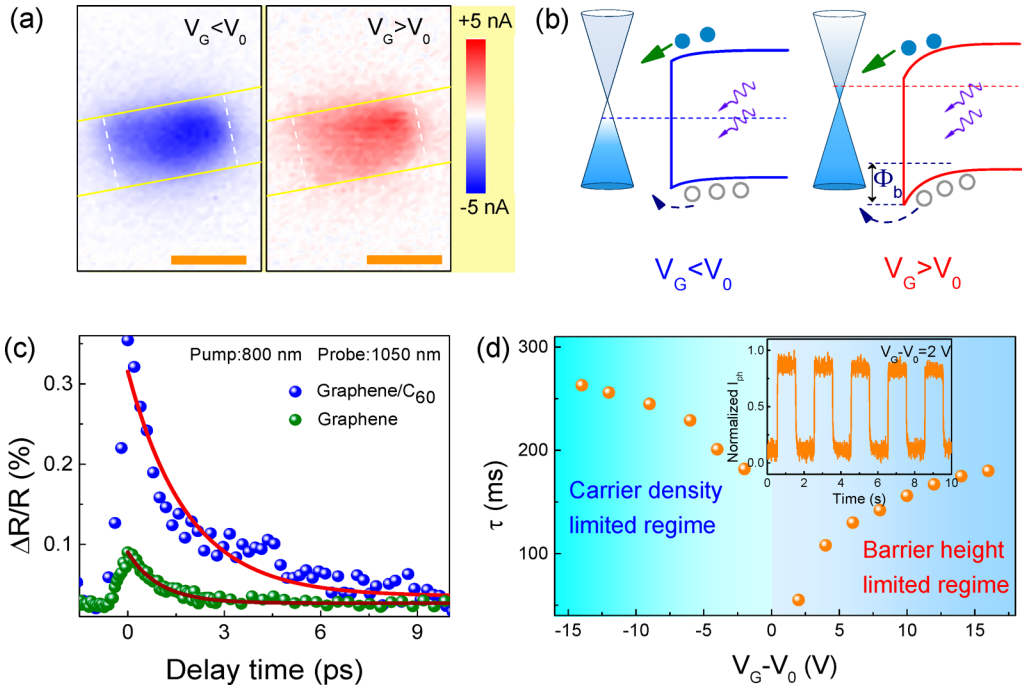

Figure 4. (a) Photocurrent image of hybrid graphene/C_{60} transistor marked in panel b at $V_G - V_0 = -5$ V (top panel) and $V_G - V_0 = 5$ V (bottom panel). The gold solid line indicates the electrode, and the white dashed line indicates the graphene/C_{60} channel. Scale bars: 20 μm. (b) Schematic band diagrams illustrating the charge-transfer dynamics at different back-gate voltage. The dash lines correspond to the Fermi level of graphene at different gate voltages. The navy dash arrows shows the photogenerated-hole recombination (photocurrent decay) process after laser pulse is off. Φ_b represents the potential barrier height. (c) Differential reflection ($\Delta R/R_0$) measured from pristine monolayer graphene and graphene/C_{60} heterointerface with a 800 nm pump and a 1050 nm probe pulse. Red lines are the fitting curves. (d) Fall time τ as a function of the gate bias V_G. Inset: temporal photocurrent response curves at $V_G - V_0 = 2$ V.

C_{60} crystal on graphene (Figures 1c and S2). An atomically flat, dangling-bond-free graphene substrate together with a highly similar lattice structure is believed to form the excellent epitaxial condition for C_{60} molecules by van der Waals interaction.[27,28] Furthermore, the planar π surface of graphene makes C_{60} self-assembly a highly effective processing through intermolecular $\pi-\pi$ stacking.[29] Such interactions can make C_{60} molecules firmly locked to the graphene lattice, leading to a strongly bonded graphene/C_{60} interface. The optical absorption spectra of the pristine graphene and the graphene/C_{60} hybrid films are shown in Figure 1d. In the UV region, four absorption peaks associated with band-to-band electronic transitions are observed at 461 nm (2.68 eV), 344 nm (3.60 eV), 267 nm (4.64 eV), and 219 nm (5.66 eV) (see details in section 3 of the Supporting Information). Importantly, the absorbance of the hybrid film is found accurately regulated by the thickness of the C_{60} constituent layer, where close-to-unity absorption can be achieved for wavelength below 300 nm with a ~75 nm thick C_{60} layer.

To investigate the charge-transfer dynamics or doping scenario of the graphene−C_{60} interface, Raman spectroscopy was performed, as shown in Figure 2a. For the pristine graphene, the prominent G (1586 cm^{-1}) and 2D (2687 cm^{-1}) peaks exhibit an intensity ratio (I_{2D}/I_G) of ~2, and the D peak is absent, confirming that the graphene sheet is monolayer with reasonably good quality.[18] Upon C_{60} (~4 nm) deposition, both G and 2D peaks are slightly up-shifted, indicating a hole doping for graphene due to phonon renormalization from nonadiabatic electron−phonon coupling (see detailed analysis in section S4 of the Supporting Information).[30] The frequency shift of the Raman peak scales linearly with the Fermi energy ($\Delta\omega_G = \Delta|E_F| \times 42$ cm^{-1} eV^{-1}; see ref 31) and the change of carrier concentration obeys $\Delta n = (\Delta|E_F|/\hbar\nu_F)^2/\pi$ (see ref 32), where $\nu_F = 1.1 \times 10^6$ m/s is the Fermi velocity. This allows us to estimate a hole-doping level on the order of 10^{12} cm^{-2}. As the C_{60} thickness increases, the 2D peaks for graphene appreciably shift up with suppressed intensities and wider full width at half maximum (fwhm), which makes the G band of graphene overlap with the high-energy $H_g(8)$ mode of the C_{60} film, as shown in the inset of Figure 2a. The role of C_{60} molecules as the electron acceptors is further corroborated by the transfer curves (Figure 2b), where the Dirac point (or, equivalently, V_D, the charge-neutrality point) shifted from 9 to 32 V following the deposition of C_{60} layer. The energy level of the Dirac point of graphene is close to the lowest unoccupied molecular orbital (LUMO) of C_{60},[26] enhancing the likelihood for electrons capture by either LUMO or unoccupied midgap trap states in C_{60} (inset of Figure 2b). The amount of electron transfer from graphene to C_{60} can be estimated by$\Delta n = C_g\Delta V/e$ to be 1.66×10^{12} cm^{-2}, which is equivalent to ~0.013 electron captured per interfacial C_{60} molecule, agreeing well with the dimer/hole configuration.[25]

Figure 3a shows the resistance of the graphene/C_{60} as a function of back-gate voltage V_G under different optical power densities (405 nm). In all cases, illumination causes the Dirac point to shift to lower values of V_G, indicating that photogenerated electrons are transferred from C_{60} into graphene (inset of Figure 3a). Because the photogenerated holes remain trapped in the C_{60} layer, a photogating effect is resulted and shifts the V_D to a lower gate bias. For $V_G < V_D$, the carrier transport in the graphene channel is hole-dominant, which can recombine with both the photogenerated electrons

DOI: 10.1021/acsami.8b11596
ACS Appl. Mater. Interfaces 2018, 10, 38326−38333

from C_{60} and photogating-induced electrons, leading to an increased resistance. In contrast, for $V_G > V_D$, the electron is the dominant charge carrier in graphene, and thus, illumination leads to a decrease of resistance. The photocurrent shows the effective tunable characteristic, which allows the control of the photoresponsivity by gate bias (see Figure S5).

The responsivity (defined as $R = I_{ph}/p_{in}$) and photocurrent measured at V_{DS} = 250 mV at different gate bias was summarized in Figure 3b. The R of our device can reach ~10^6 A/W under low light intensity (405 nm, ~5 μW/cm^2), which is comparable to or higher than that of the reported semiconducting light-absorbing layer at similar excitation intensity (see details in section S6 of the Supporting Information and Table S1).[7,8,18,33−35] As with most graphene-based phototransistors, R decreases at high incident photon densities due to the saturated absorption and the weakened built-in field.[7] It is noted that the device shows different photoresponsivity−power density decay relations at different gate bias, which is universal in graphene-based photodetectors.[7,8] This phenomenon results from the hole and electron mobility difference of graphene and the additional conductivity of C_{60} under illumination. The external quantum efficiency (EQE, $\eta_{EQE} = Rhv/e$) is also calculated (Figure S7). We attribute the superior EQE in graphene−C_{60} interfaces to strong UV light absorption in the C_{60} film as well as the intimate sp^2-hybridized interface.[18] The linear scaling of the photocurrent with the bias V_{DS} for different optical powers at V_G = 0 V is clearly observed (see Figure S8). The characterization of the microscopic morphology and photoresponse for the same graphene/C_{60} phototransistor demonstrate that such hybrid devices have excellent long-term stability. For example, there is no obvious difference in the device response between an as-fabricated device and a device after 2 month of operation (Figure 3c,d). These results are especially relevant for the practical applications. In addition, the dependence of photocurrent on C_{60} film thickness was also studied, as plotted in Figure 3e. The photocurrents first increase and then gradually become saturated as the C_{60} thickness increase, implying that photoresponse is mainly dominated by C_{60} molecules near the heterointerface. The internal quantum efficiency (IQE) decreases as the C_{60} thickness increases (inset of Figure 3e), but it still remains as high as 2.0 × 10^4 in all devices, even at relatively high laser power density (5 mW/cm^2).

To further verify the photocurrent generation mechanism in the graphene/C_{60} heterostructure, high-resolution spatial photocurrent mapping was employed under a confocal optical microscope (see the Experimental section for details). To avoid any organic residue and preserve a clean graphene−C_{60} interface, the Au electrodes were mechanically transferred onto an exfoliated graphene sheet without lithography. The optical images and the corresponding transfer curves in dark/light of pristine graphene and graphene/C_{60} hybrid transistor are shown in Figures S9 and S10. For ease of discussion, we define the cross-point between the transfer curves under dark and illumination to be V_0. The photocurrent mapping results at the two different back-gate regimes are shown in Figure 4a, in which the different polarity of the photocurrent are consistent with the photogating effect. Photocurrent generation clearly arises from the graphene/C_{60} hybrid channel rather than electrode/channel junctions or other regions, excluding the thermoelelectric effect as the main contribution.[36] The temperature dependence of I_{DS} allows us to neglect the bolometric contribution (see Figure S11). In particular, the electrostatically tuned work function of graphene allows us to regulate the energy barrier (or band alignment) at the graphene−C_{60} interfaces, as illustrated in Figure 4b. For $V_G > V_0$, the built-in electric field at the graphene−C_{60} interface gets enhanced, which facilitates electron−hole pair separation, leading to increased photoresponsivity. To reveal the intrinsic photoexcited carrier dynamics, we perform ultrafast pump−probe spectroscopy of the graphene−C_{60} interface (see the Experimental section). A 800 nm pulse is selected to pump the C_{60} layer, and a 1050 nm pulse is used to probe the state filling caused by charge transfer in graphene only. The time-resolved differential reflection ($\Delta R/R_0$) for the graphene−C_{60} heterointerface is shown as the blue circles in Figure 4c. The magnitude of the signal is 4 times higher than the individual graphene samples (olive circles) with a single-exponential decay (red curve, ~1.8 ps). For a 550/800 nm pump/probe pulse, the signal decays bi-exponentially with a fast time constant of 3.8 ps and a slow constant of 48 ps, in which the slow component is reasonably consistent with the photocarrier lifetime in C_{60} (for details, see section 12 in the Supporting Information). These transient measurements provide unambiguous evidence of the ultrafast and efficient transfer of photocarriers; that is, most photogenerated carriers in C_{60} transfer to graphene and recombine within a time scale of a few picoseconds.

We then investigate the device response speed. The rise time of the detector is reasonably fast (<5 ms), while the decay time is longer (~55 ms at $V_G - V_0$ = 2 V; see the inset of Figure 4d). The multiple trap states, i.e., disorder or defects, and low-mobility interlayer hopping of trapped carriers in C_{60} are responsible for the slow release times.[6] It is noted that the decay time (τ) can be modulated by the back-gate voltage, i.e., the response time is fastest when V_G is around V_0, and it will gradually increase when V_G is tuned away from V_0. There is a noticeable difference in the two V_G regimes; that is, an overall faster decay time for $V_G > V_0$ and a slower decay regime for $V_G < V_0$ (Figure 4d). Such an asymmetric effect is believed to arise from the photogenerated-hole recombination process near the graphene−C_{60} interface.[7,37] For $V_G < V_0$, the hole-rich channel hampers the photogenerated-hole diffusion from C_{60}, resulting in a slow interfacial recombination process, as illustrated in Figure 4b. As the magnitude of negative V_G increases, the higher density of holes in graphene prolongs such a recombination process. However, for $V_G > V_0$, a high density of electrons in graphene can shorten the lifetime of photogenerated holes trapped in C_{60}. While increasing the positive V_G values would raise the potential barrier Φ_b (see Figure 4b), it blocks the escape of photogenerated holes to the graphene channel, increasing the decay time. That is to say that the recombination process is mainly limited by the hole carrier density in graphene for $V_G < V_0$, while it is limited by the potential barrier height for $V_G > V_0$.

The long lifetime of holes localized in C_{60} leads to a high photoconductive gain ($G = \tau_{life}/\tau_{tr}$), which originates from the multiple electrons recirculation in the graphene transistor. For a bias voltage V_{DS} of 250 mV and a measured field-effect mobility of 3800 cm^2 V^{-1} s^{-1} (Figure S10), the transit time is estimated to be $\tau_{tr} = L^2/\mu V_{DS}$. A gain range of 8.5 × 10^6−4 × 10^7 is calculated using lifetime of 55 and 260 ms respectively, which provides an amplification function for the photoresponsivity. For the specific CVD-graphene/C_{60} device, the gain is also on the order of 4 × 10^7 using lifetime of 200 ms

DOI: 10.1021/acsami.8b11596
ACS Appl. Mater. Interfaces 2018, 10, 38326−38333

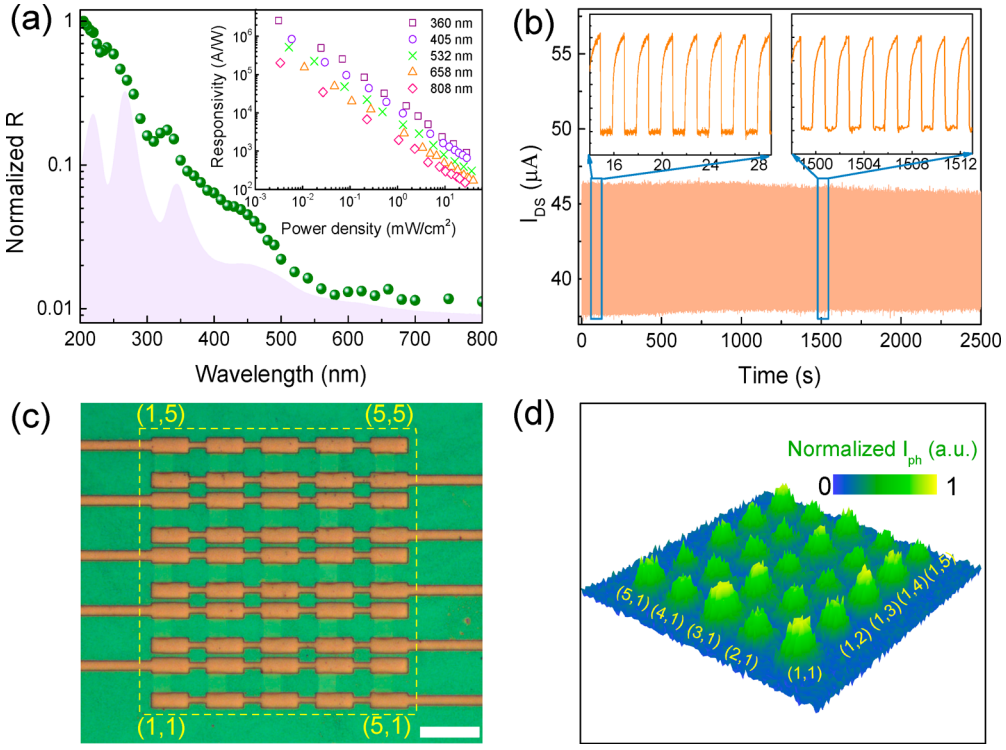

Figure 5. (a) Normalized spectral responsivity of the hybrid device. Red shaded areas correspond to the absorption of the hybrid film. Inset: responsivities as a function of the optical power density for several UV and visible laser diodes (360, 405, 532, 658, and 808 nm). (b) Highly reproducible photocurrent response curves for >1200 cycles at ambient conditions, measured at $V_G - V_0 = -10$ V and $V_{SD} = 10$ mV with an incident power of 0.35 mW/cm^2. (c) Optical microscope image of a 5 × 5 integrated array. Scale bar: 10 μm. (d) The spatial-light mapping for the arrayed devices.

and mobility of 3100 cm^2 V^{-1} s^{-1} (Figure 3a). Therefore, the gain-bandwidth product of our all-carbon hybrid device is on the order of 2 × 10^8 Hz, which is quantitatively similar or better to other graphene-based hybrid photodetector.

To confirm the capability of such an all-carbon hybrid film as UV photodetectors, we measured the broadband photoresponse of our device from 200 to 800 nm. As shown in Figure 5a, higher responsivity is achieved for the UV band, which is consistent with the absorption of the hybrid film. The responsivity is also measured by using several UV and visible laser diodes (inset of Figure 5a). At an illumination power density of ∼2.5 μW/cm^2, all wavelengths exhibit a responsivity of >10^5 A/W. From the spectrum responsivity, we deduce a photoresponsivity of ∼3 × 10^7 A/W for 200 nm illumination. For ∼2.0 eV band gap of C_{60}, the long absorption tail extending into the energy gap is as a result of structural or compositional disorder,[38] which is responsible for the response at long wavelength range (>620 nm). Such all-carbon devices exhibit robust switching behavior and excellent reproducibility. Even at ambient condition, the device keeps a good responsivity without any degradation after thousands of cycles (Figure 5b). Drawing on the large-area growth, transfer of CVD graphene and scalable processability of C_{60}, the hybrid films allow for facile and scaled-up processing. Figure 5c shows the optical image for an exemplary 5 × 5 integrated array. The spatial light mapping for the devices array is shown in Figure 5d, in which the arrayed devices exhibit a rather uniform photoresponse, opening up the potential for large-scale integration.

CONCLUSIONS

In summary, we report herein a large-area graphene/C_{60} hybrid film with strong and tunable UV absorption, and the charge-transfer dynamics at the interface are systematically probed. The film is subsequently used to demonstrate an ultrasensitive UV photodetector with a responsivity exceeding 10^7 A/W. Due to the high mobility of graphene and the well-organized assembly of C_{60} molecules, the device features fast and gate-dependent transient characteristics. Harnessing the excellent long-term stability, high reliability, and scalable processability, a 5 × 5 photodetector array is successfully fabricated. Our results significantly improve the performance level of a graphene-based UV photodetector. The efficient electronic coupling of such an all-carbon interface may pave the way for other optoelectronic functionalities such as light emission and solar-harnessing applications.

ASSOCIATED CONTENT

Supporting Information

The Supporting Information is available free of charge on the ACS Publications website at DOI: 10.1021/acsami.8b11596.

Additional experimental and characterization details and figures (PDF)

AUTHOR INFORMATION

Corresponding Authors

*E-mail: fwang@nju.edu.cn.
*E-mail: rzhang@nju.edu.cn.

ORCID

Xinran Wang: 0000-0002-3975-1667

DOI: 10.1021/acsami.8b11596
ACS Appl. Mater. Interfaces 2018, 10, 38326−38333

Kaihui Liu: 0000-0002-8781-2495
Fengqiu Wang: 0000-0001-9823-5788

Notes

The authors declare no competing financial interest.

■ ACKNOWLEDGMENTS

This work was supported in part by National Basic Research Program of China (grant nos. 2017YFA0206304 and 2014CB921101), National Natural Science Foundation of China (grant nos. 61775093, 61378025, 61427812, 61274102, and 61504056), and the National Youth 1000-Talent Plan; A "Jiangsu Shuangchuang Team" Program.

■ REFERENCES

(1) Liu, C. H.; Chang, Y. C.; Norris, T. B.; Zhong, Z. Graphene Photodetectors with Ultra-Broadband and High Responsivity at Room Temperature. *Nat. Nanotechnol.* **2014**, *9*, 273−278.
(2) Koppens, F. H.; Mueller, T.; Avouris, P.; Ferrari, A. C.; Vitiello, M. S.; Polini, M. Photodetectors based on Graphene, Other Two-Dimensional Materials and Hybrid Systems. *Nat. Nanotechnol.* **2014**, *9*, 780−793.
(3) Mak, K. F.; Shan, J.; Heinz, T. F. Seeing Many-Body Effects in Single- and Few-Layer Graphene: Observation of Two-Dimensional Saddle-Point Excitons. *Phys. Rev. Lett.* **2011**, *106*, 046401.
(4) Nikitskiy, I.; Goossens, S.; Kufer, D.; Lasanta, T.; Navickaite, G.; Koppens, F. H.; Konstantatos, G. Integrating an Electrically Active Colloidal Quantum Dot Photodiode with a Graphene Phototransistor. *Nat. Commun.* **2016**, *7*, 11954.
(5) Georgiou, T.; Jalil, R.; Belle, B. D.; Britnell, L.; Gorbachev, R. V.; Morozov, S. V.; Kim, Y. J.; Gholinia, A.; Haigh, S. J.; Makarovsky, O.; Eaves, L.; Ponomarenko, L. A.; Geim, A. K.; Novoselov, K. S.; Mishchenko, A. Vertical Field-Effect Transistor based on Graphene-WS_2 Heterostructures for Flexible and Transparent Electronics. *Nat. Nanotechnol.* **2013**, *8*, 100−103.
(6) Liu, X.; Luo, X.; Nan, H.; Guo, H.; Wang, P.; Zhang, L.; Zhou, M.; Yang, Z.; Shi, Y.; Hu, W.; Ni, Z.; Qiu, T.; Yu, Z.; Xu, J. B.; Wang, X. Epitaxial Ultrathin Organic Crystals on Graphene for High-Efficiency Phototransistors. *Adv. Mater.* **2016**, *28*, 5200−5205.
(7) Konstantatos, G.; Badioli, M.; Gaudreau, L.; Osmond, J.; Bernechea, M.; de Arquer, F. P. G.; Gatti, F.; Koppens, F. H. Hybrid Graphene-Quantum Dot Phototransistors with Ultrahigh Gain. *Nat. Nanotechnol.* **2012**, *7*, 363−368.
(8) Shao, Y.; Liu, Y.; Chen, X.; Chen, C.; Sarpkaya, I.; Chen, Z.; Fang, Y.; Kong, J.; Watanabe, K.; Taniguchi, T.; Taylor, A.; Huang, J.; Xia, F. Stable Graphene-Two-Dimensional Multiphase Perovskite Heterostructure Phototransistors with High Gain. *Nano Lett.* **2017**, *17*, 7330−7338.
(9) Liu, S.; Liao, Q.; Lu, S.; Zhang, Z.; Zhang, G.; Zhang, Y. Strain Modulation in Graphene/ZnO Nanorod Film Schottky Junction for Enhanced Photosensing Performance. *Adv. Funct. Mater.* **2016**, *26*, 1347−1353.
(10) Mehew, J. D.; Unal, S.; Torres Alonso, E.; Jones, G. F.; Fadhil Ramadhan, S.; Craciun, M. F.; Russo, S. Fast and Highly Sensitive Ionic-Polymer-Gated WS_2 -Graphene Photodetectors. *Adv. Mater.* **2017**, *29*, 1700222.
(11) Zhang, X.; Liao, Q.; Liu, S.; Kang, Z.; Zhang, Z.; Du, J.; Li, F.; Zhang, S.; Xiao, J.; Liu, B.; Ou, Y.; Liu, X.; Gu, L.; Zhang, Y. Poly(4-styrenesulfonate)-induced Sulfur Vacancy Self-Healing Strategy for Monolayer MoS_2 Homojunction Photodiode. *Nat. Commun.* **2017**, *8*, 15881.
(12) Zayat, M.; Garcia-Parejo, P.; Levy, D. Preventing UV-light Damage of Light Sensitive Materials Using a Highly Protective UV-absorbing Coating. *Chem. Soc. Rev.* **2007**, *36*, 1270−1281.
(13) Guo, W.; Xu, S.; Wu, Z.; Wang, N.; Loy, M. M. T.; Du, S. Oxygen-Assisted Charge Transfer Between ZnO Quantum Dots and Graphene. *Small* **2013**, *9*, 3031−3036.
(14) Babichev, A. V.; Zhang, H.; Lavenus, P.; Julien, F. H.; Egorov, A. Y.; Lin, Y. T.; Tu, L. W.; Tchernycheva, M. GaN Nanowire Ultraviolet Photodetector with a Graphene Transparent Contact. *Appl. Phys. Lett.* **2013**, *103*, 201103.
(15) Kong, W. Y.; Wu, G. A.; Wang, K. Y.; Zhang, T. F.; Zou, Y. F.; Wang, D. D.; Luo, L. B. Graphene-β-Ga_2O_3 Heterojunction for Highly Sensitive Deep UV Photodetector Application. *Adv. Mater.* **2016**, *28*, 10725−10731.
(16) Chu, J.; Wang, F.; Yin, L.; Lei, L.; Yan, C.; Wang, F.; Wen, Y.; Wang, Z.; Jiang, C.; Feng, L.; Xiong, J.; Li, Y.; He, J. High-Performance Ultraviolet Photodetector based on a Few-Layered 2D $NiPS_3$ Nanosheet. *Adv. Funct. Mater.* **2017**, *27*, 1701342.
(17) Zhang, Y.; Yan, X.; Yang, Y.; Huang, Y.; Liao, Q.; Qi, J. Scanning Probe Study on the Piezotronic Effect in ZnO Nanomaterials and Nanodevices. *Adv. Mater.* **2012**, *24*, 4647−4655.
(18) Liu, Y.; Wang, F.; Wang, X.; Wang, X.; Flahaut, E.; Liu, X.; Li, Y.; Wang, X.; Xu, Y.; Shi, Y.; Zhang, R. Planar Carbon Nanotube-Graphene Hybrid Films for High-Performance Broadband Photodetectors. *Nat. Commun.* **2015**, *6*, 8589.
(19) Liu, Y.; Liu, Y.; Qin, S.; Xu, Y.; Zhang, R.; Wang, F. Graphene-Carbon Nanotube Hybrid Films for High-Performance Flexible Photodetectors. *Nano Res.* **2017**, *10*, 1880−1887.
(20) Qin, S.; Wang, F.; Liu, Y.; Wan, Q.; Wang, X.; Xu, Y.; Shi, Y.; Wang, X.; Zhang, R. A Light-Stimulated Synaptic Device based on Graphene Hybrid Phototransistor. *2D Mater.* **2017**, *4*, 035022.
(21) Wang, R.; Wang, S.; Wang, X.; Meyer, J. A.; Hedegard, P.; Laursen, B. W.; Cheng, Z.; Qiu, X. Charge Transfer and Current Fluctuations in Single Layer Graphene Transistors Modified by Self-Assembled C_{60} Adlayers. *Small* **2013**, *9*, 2420−2426.
(22) Du, L.; Luo, X.; Zhao, F.; Lv, W.; Zhang, J.; Peng, Y.; Tang, Y.; Wang, Y. Toward Facile Broadband High Photoresponse of Fullerene based Phototransistor from the Ultraviolet to the Near-Infrared Region. *Carbon* **2016**, *96*, 685−694.
(23) Luo, X.; Du, L.; Lv, W.; Sun, L.; li, Y.; Peng, Y.; Zhao, F.; Zhang, J.; Tang, Y.; Wang, Y. Charge-Transport Interfacial Modification Enhanced Ultraviolet (UV)/Near-UV Phototransistor with High Sensitivity and Fast Response Speed. *Synth. Met.* **2015**, *210*, 230−235.
(24) Yang, D.; Xu, K.; Zhou, X.; Wang, Y.; Ma, D. Comprehensive Studies of Response Characteristics of Organic Photodetectors based on Rubrene and C_{60}. *J. Appl. Phys.* **2014**, *115*, 244506.
(25) Ojeda-Aristizabal, C.; Santos, E. J. G.; Onishi, S.; Yan, A.; Rasool, H. I.; Kahn, S.; Lv, Y.; Latzke, D. W.; Velasco, J., Jr.; Crommie, M. F.; Sorensen, M.; Gotlieb, K.; Lin, C. Y.; Watanabe, K.; Taniguchi, T.; Lanzara, A.; Zettl, A. Molecular Arrangement and Charge Transfer in C_{60}/Graphene Heterostructures. *ACS Nano* **2017**, *11*, 4686−4693.
(26) Jnawali, G.; Rao, Y.; Beck, J. H.; Petrone, N.; Kymissis, I.; Hone, J.; Heinz, T. F. Observation of Ground- and Excited-State Charge Transfer at the C_{60}/Graphene Interface. *ACS Nano* **2015**, *9*, 7175−7185.
(27) Švec, M.; Merino, P.; Dappe, Y. J.; González, C.; Abad, E.; Jelínek, P.; Martín-Gago, J. A. Van der Waals Interactions Mediating the Cohesion of Fullerenes on Graphene. *Phys. Rev. B: Condens. Matter Mater. Phys.* **2012**, *86*, 121407.
(28) Cho, J.; Smerdon, J.; Gao, L.; Suzer, O.; Guest, J. R.; Guisinger, N. P. Structural and Electronic Decoupling Of C_{60} from Epitaxial Graphene On SiC. *Nano Lett.* **2012**, *12*, 3018−3024.
(29) Zhang, Z.; Huang, H.; Yang, X.; Zang, L. Tailoring Electronic Properties of Graphene by π-π Stacking with Aromatic Molecules. *J. Phys. Chem. Lett.* **2011**, *2*, 2897−2905.
(30) Das, A.; Pisana, S.; Chakraborty, B.; Piscanec, S.; Saha, S. K.; Waghmare, U. V.; Novoselov, K. S.; Krishnamurthy, H. R.; Geim, A. K.; Ferrari, A. C.; Sood, A. K. Monitoring Dopants by Raman Scattering in An Electrochemically Top-Gated Graphene Transistor. *Nat. Nanotechnol.* **2008**, *3*, 210−215.
(31) Chen, C. F.; Park, C. H.; Boudouris, B. W.; Horng, J.; Geng, B.; Girit, C.; Zettl, A.; Crommie, M. F.; Segalman, R. A.; Louie, S. G.;

DOI: 10.1021/acsami.8b11596
ACS Appl. Mater. Interfaces 2018, 10, 38326−38333

Wang, F. Controlling Inelastic Light Scattering Quantum Pathways in Graphene. *Nature* **2011**, *471*, 617−620.
(32) Zhang, Y.; Tan, Y. W.; Stormer, H. L.; Kim, P. Experimental Observation of the Quantum Hall Effect and Berry's Phase in Graphene. *Nature* **2005**, *438*, 201−204.
(33) Sun, Z.; Liu, Z.; Li, J.; Tai, G. A.; Lau, S. P.; Yan, F. Infrared Photodetectors Based on CVD-Grown Graphene and PbS Quantum Dots with Ultrahigh Responsivity. *Adv. Mater.* **2012**, *24*, 5878−5883.
(34) Jones, G. F.; Pinto, R. M.; De Sanctis, A.; Nagareddy, V. K.; Wright, C. D.; Alves, H.; Craciun, M. F.; Russo, S. Highly Efficient Rubrene-Graphene Charge-Transfer Interfaces as Phototransistors in the Visible Regime. *Adv. Mater.* **2017**, *29*, 1702993.
(35) Xu, H.; Wu, J.; Feng, Q.; Mao, N.; Wang, C.; Zhang, J. High Pesponsivity and Gate Tunable Graphene-MoS_2 Hybrid Photo-transistor. *Small* **2014**, *10*, 2300−2306.
(36) Xia, F.; Mueller, T.; Golizadeh-Mojarad, R.; Freitag, M.; Lin, Y.-m.; Tsang, J.; Perebeinos, V.; Avouris, P. Photocurrent Imaging and Efficient Photon Detection in a Graphene Transistor. *Nano Lett.* **2009**, *9*, 1039−1044.
(37) Chen, X.; Liu, X.; Wu, B.; Nan, H.; Guo, H.; Ni, Z.; Wang, F.; Wang, X.; Shi, Y.; Wang, X. Improving the Performance of Graphene Phototransistors Using a Heterostructure as the Light-Absorbing Layer. *Nano Lett.* **2017**, *17*, 6391−6396.
(38) Wang, Y.; Holden, J. M.; Rao, A. M.; Eklund, P. C.; Venkateswaran, U. D.; Eastwood, D.; Lidberg, R. L.; Dresselhaus, G.; Dresselhaus, M. S. Optical Absorption and Photoluminescence in Pristine and Photopolymerized C_{60} Solid Films. *Phys. Rev. B: Condens. Matter Mater. Phys.* **1995**, *51*, 4547−4556.

DOI: 10.1021/acsami.8b11596
ACS Appl. Mater. Interfaces 2018, 10, 38326−38333